Supplementary Information

Machine Learning Driven Discovery of Low Modulus Biomedical Titanium Alloys for Additive Manufacturing

Jinlong Su, Fulin Jiang, Jin Wu, Yuehua Li, Ri Han, Lu Wang, Raymond Chung Wen Wong, Jian Wang, Swee Leong Sing

Supplementary Notes

Supplementary Note 1. Alloy design-related supplementary information

For the CALPHAD simulations, titanium (Ti) was selected as the base element, with niobium (Nb) and tantalum (Ta) varied from 0 to 30 wt.% in 6 wt.% increments, and zirconium (Zr) and tin (Sn) varied from 0 to 10 wt.% in 5 wt.% increments. In total, 320 compositions were calculated using the Scheil module in the Thermo-Calc software with TCTI1 database. The classical Scheil solidification model was adopted and all elements were treated as normal elements without fast diffusers. The solidification freezing range (*SFR*), hot cracking susceptibility (*HCS*), and growth restriction factor (*GRF*) data were extracted from the Scheil curves based on the Equation 1–3. The corresponding schematic diagram is provided in Supplementary Figure 1.

$$SFR = T_{max} - T_{min} \tag{1}$$

$$HCS = \frac{t(x = 1.0) - t(x = 0.9)}{t(x = 0.9) - t(x = 0.4)} \tag{2}$$

$$GRF = \left| \frac{y(x = 0.05) - y(x = 0)}{0.05} \right| \tag{3}$$

Hyperparameter tuning of the ML surrogate models was performed using a grid-search strategy over predefined ranges for each algorithm, as summarised in Table S1. In all cases, the final hyperparameters were selected based on their ability to simultaneously maximise R^2 and minimise MAE under 5-fold cross-validation. Supplementary Figure 2 presents the predicted versus actual values for the various machine learning (ML) surrogate models applied to HCS, GRF, and SFR. Each subplot displays a regression analysis, where the closer the predicted values (indicated by red dots) align with the diagonal blue line, the better the model's performance. The green tick highlights the optimal models for each property, demonstrating their effectiveness, particularly the RF model for HCS and SFR, and the KNN model for GRF, as evidenced by their lower mean absolute error (MAE) and higher R^2 scores.

Supplementary Figure 3 presents data for the two phenomenological models within the alloy design framework. In Supplementary Figure 3a, a linear correlation is observed between grain size and the inverse GRF for various laser powder bed fusion (LPBF)-produced titanium alloys, modelled by a phenomenological equation that achieves a high R^2 value of 0.906. Supplementary Figure 3b illustrates the exponential relationship between the critical current density for passivation (*Ip*) and the compositional average bond order (*Bo*), with a robust fit (R^2 = 0.958) highlighting the predictive capability of bond order in assessing corrosion

resistance. These phenomenological models have been integrated into the alloy design framework to enhance the construction of composition-property relationships.

Supplementary Figure 4 presents a scatter plot matrix of the Pareto front derived from the non-dominated sorting genetic algorithm II (NSGA-II), revealing a strong positive correlation between yield strength (*YS*) and peak anodic current density (*Ip*), as well as between -*SFR* and *HCS*. To avoid overweighting highly correlated objectives, we grouped (*YS*, *Ip*) and (*SFR*, *HCS*) as two coupled criteria and assigned equal weight to each group and to BF, resulting in weights of 1/6 for *YS*, *Ip*, *SFR* and *HCS*, and 1/3 for *BF*. Such a weighting scheme ensures a balanced consideration of both interrelated properties and the distinct importance of *BF*, enabling a comprehensive assessment in the alloy design framework. Following this analysis, a further TOPSIS selection was conducted, and the ANTZS alloy (Ti-15.8Nb-9.2Ta-10.0Zr-7.7Sn) is thus designed.

Supplementary Figure 5 provides a two-dimensional comparison of the designed ANTZS alloy against the entire Ti-*x*Nb-*y*Ta-*z*Zr-*w*Sn alloy composition space, where the black dots represent all considered alloy compositions within the specified ranges (x = 0–30 wt%, y = 0–30 wt%, z = 0–10 wt%, and w = 0–10 wt%). The yellow star highlights the TOPSIS-selected optimal composition (i.e., the ANTZS alloy), indicating that the ANTZS alloy exhibits exceptional and balanced performance across five key objectives (i.e., *YS*, *HCS*, *SFR*, *Ip* and *BF*), positioning it favourably for biomedical AM applications compared to other Ti-Nb-Ta-Zr-Sn alloys in the vast composition space.

Supplementary Note 2. Printability-related supplementary information

The representative morphologies of single-track samples, along with their corresponding melt pool cross-sections (Supplementary Figure 6), reveal a transition from lack-of-fusion defects at low energy inputs (with a linear energy density of 0.13 J/mm) to keyhole-induced porosity at excessively high energy inputs (with a linear energy density of 1.6 J/mm). Building on the single-track printing findings, bulk samples were printed using laser powers of 200-400 W and scan speeds of 500-1500 mm/s, which allowed for a comprehensive exploration of the printability and the full property potential of the designed ANTZS alloy.

Supplementary Figure 7 & Supplementary Figure 8 show light optical microscopy (OM) images of polished cross-sections of the designed ANTZS alloy and conventional Ti64 bulk samples fabricated under different LPBF process parameters. For both alloys, under high laser power combined with low scan speeds (e.g., 400 W & 500 mm/s), keyholing pores are obvious. Besides, lower laser powers with higher scan speeds (e.g., 200 W & 1500 mm/s) lead to irregular lack-of-fusion defects. Notably, the Ti64 alloy (Supplementary Figure 8) shows a greater susceptibility to the formation of keyholing pores under high energy densities. In other words, the optimal process window for the ANTZS alloy is situated in a higher energy density area compared to the Ti64 alloy, which can be attributed to differing physical properties of the two alloys including melting point, thermal conductivity, and specific heat capacity, etc.

Supplementary Note 3. Microstructure and properties-related supplementary information

Supplementary Figure 9 illustrates the mechanical properties of LPBF-built ANTZS alloys under various process parameters. Tensile tests conducted on these LPBF-built ANTZS alloys reveal that the Young's modulus decreases with increasing volumetric energy density (VED), while elongation shows an upward trend with rising VED. By increasing the VED within an appropriate range, the Young's modulus can be reduced and the ductility can be enhanced simultaneously, resulting in superior performance compared with both the as-cast and spark plasma–sintered (SPS) states.

Supplementary Figure 10 presents the fracture morphologies of LPBF-built ANTZS alloys produced under different laser powers and scanning speeds. Overall, all samples exhibit a ductile fracture mode, characterized by the presence of dimples across the morphologies. Notably, the samples fabricated with highest VED (P = 400 W, v = 750 mm/s) display deepest dimples, which consistent with the highest ductility measured for this condition.

As dictated in Figure 6a of the main text, the as-cast ANTZS alloy exhibits a tensile deformation behavior distinctly different from that of the LPBF-built ANTZS alloy, characterized by a double-yielding phenomenon. This behavior can be attributed to the α″ + β dual-phase microstructure of the as-cast alloy, in contrast to the single metastable β-phase microstructure of the LPBF-built alloy. XRD analysis in Supplementary Figure 11a reveals a clear reduction in β-phase peak intensity after tensile fracture in the as-cast ANTZS alloy, indicating the occurrence of strain-induced martensitic transformation (β→α″) during tensile test. Consistently, EBSD phase mapping of the fractured as-cast ANTZS sample confirms extensive formation of strain-induced α″ martensite (Supplementary Figure 11c). Prior to yielding, it can be inferred that both β and α″ phases elastically share the applied load, while the first yielding is primarily associated with irreversible deformation in the β matrix accompanied by the onset of β→α″ transformation. The progressive martensitic transformation and the resulting increase in β/α″ interfacial constraints enhance work hardening, giving rise to the double-yielding behavior. In contrast, the LPBF ANTZS alloy retains a predominantly single-phase β microstructure before and after fracture (Supplementary Figure 11a and b), indicating suppressed strain-induced martensitic transformation and resulting in a smooth, single-yield tensile response.

The EBSD IPF maps of LPBF-built ANTZS alloys are presented in Supplementary Figure 12. For quantitatively analysis the texture, the degree of <001> orientation ($p_{<001>}$) with respect to the build direction (BD) was determined from the Euler angles at each measurement point. The $p_{<001>}$ is estimated based on the following equation:

$$p_{<001>} = \langle cos^2 \alpha_{<001>} \rangle \quad \text{(S4)}$$

The $\alpha_{<001>}$ is defined as the smallest angle between the observation direction and the equivalent orientations of <001>.

The (100) pole figures of LPBF-built ANZTS alloys fabricated under varying process parameters were presented in Supplementary Figure 13. Obviously, the <100>//BD texture becomes more pronounced with increasing volumetric energy density (i.e., higher laser power and lower scan speed). At P = 400 W and v = 750 mm/s, a strong cubic texture (<001> // X, Y, Z) is formed, contributing to a superior low modulus along these three directions.

Supplementary Figure 14a illustrates the mechanism of cubic texture formation in the LPBF-built ANTZS alloy under high energy density conditions (e.g., P = 400 W, v = 750 mm/s). The 90° interlayer rotation (zigzag) scan strategy promotes the formation of the favourable crystallographic alignments. Supplementary Figure 14b presents the loading orientation-dependent Young's modulus of the LPBF-built ANTZS alloy, demonstrating that the modulus varies based on the loading direction. As the <001> crystallographic family aligns along the X, Y, and Z axes, the cubic texture enhances the material's advantageous low modulus characteristics in all three directions.

Supplementary Figure 15 illustrates the microstructure and mechanical properties of the ANTZS alloy fabricated by spark plasma sintering (SPS). The IPF orientation map in Supplementary Figure 15a reveals an equiaxed grain structure, and the corresponding pole figures in Supplementary Figure 15b indicate a weak <001>//pressure direction texture. The XRD pattern in Supplementary Figure 15c confirms the formation of a single β-phase microstructure in the as-SPS sample. As shown in Supplementary Figure 15d, the SPS-fabricated ANTZS sample exhibits higher strength (760.4 ± 2.5 MPa) compared to the LPBF-built and as-cast ANTZS alloys. The fracture surface shown in Supplementary Figure 15d displays ductile features, supporting the alloy's good ductility under SPS processing.

Notably, with respect to elastic modulus, the differences among the SPS-fabricated, as-cast, and LPBF-built ANTZS alloys can be attributed to the combined effects of crystallographic texture, phase constitution, and porosity. The SPS ANTZS alloy exhibits an equiaxed grain structure with a relatively weak ⟨001⟩ texture, resulting in a more orientation-averaged elastic response and therefore a higher elastic modulus compared with the LPBF ANTZS alloy. Although the SPS sample also possesses a single β-phase microstructure, the absence of a strong low-modulus ⟨001⟩ texture limits further modulus reduction. In contrast, the as-cast ANTZS alloy contains an α″ + β dual-phase microstructure, in which the presence of α″

martensite intrinsically increases the elastic modulus. For the LPBF-built ANTZS alloy, the synergy of a strong cubic ⟨001⟩ texture, a single metastable β-phase microstructure, and minor process-induced keyholing porosity contributes to the lowest elastic modulus among the three processing routes.

Supplementary Figure 16 illustrates the dislocation densities of the LPBF-fabricated ANTZS alloys prepared under varying process parameters. In Supplementary Figure 16a and b, the XRD patterns indicate that the full width at half maximum (FWHM) of the (200) peak decreases with increasing VED, suggesting a decrease in dislocation density (or an increase in grain size). As indicated by the EBSD IPF orientation maps shown in Supplementary Figure 12, the grain sizes across the samples are comparable, implying that the peak broadening is primarily due to the increased dislocation density. Supplementary Figure 16c-e showcase bright-field TEM images of the low VED sample (VED = 53.3 J·mm^{-3}), demonstrating a higher density of dislocations and the presence of α" martensite, which may result from strain-induced phase transformation during cyclic thermal loading of LPBF. Conversely, the bright-field TEM images of the high VED sample (VED = 177.8 J·mm^{-3}) in Supplementary Figure 16f-h show a more uniform distribution of dislocations, potentially contributing to improved work-hardening behavior due to reduced dislocation interactions.

Supplementary Figure17a–c compares the electrochemical corrosion behaviour of LPBF-built Ti64 and ANTZS alloys in the 0.9 wt% NaCl solution. The polarization curves in Supplementary Figure17a show that the LPBF ANTZS alloy exhibits a slightly more negative corrosion potential (E_{corr}) and a slightly higher corrosion current density (i_{corr}) than Ti64, indicating a slightly higher corrosion rate. Specifically, the corrosion current densities for the LPBF-built ANTZS and Ti64 alloys are 0.0215 and 0.0113 μA cm^{-2}, respectively. Consistently, the Nyquist plots in Supplementary Figure17b reveal a smaller semicircle diameter for ANTZS, corresponding to a lower charge-transfer resistance (R_t) and thus a less protective passive film. The Bode plots in Supplementary Figure17c further confirm this trend, as ANTZS displays a lower impedance magnitude (|Z|) across the frequency range, although both alloys maintain a capacitive phase angle of about 70–80° (Supplementary Figure17d), suggesting that each forms a stable TiO_2-based oxide film. Overall, the results indicate that LPBF Ti64 possesses relatively better corrosion resistance compared with LPBF ANTZS. The relatively lower corrosion resistance observed for LPBF ANTZS likely originates from factors not captured by the composition-only ML inputs, such as: (i) difference in passive-film nucleation and growth kinetics associated with β-dominated ANTZS versus α′-dominated Ti64; (ii) LPBF-induced texture and residual stress; and (iii) minor porosity difference. Although the corrosion

resistance of ANTZS is slightly lower than that of Ti64, the LPBF-built ANTZS still exhibits a low i_{corr} (0.0215 μA cm^{-2}) and stable passivation behaviour, supporting its suitability for biomedical applications.

Supplementary Figures

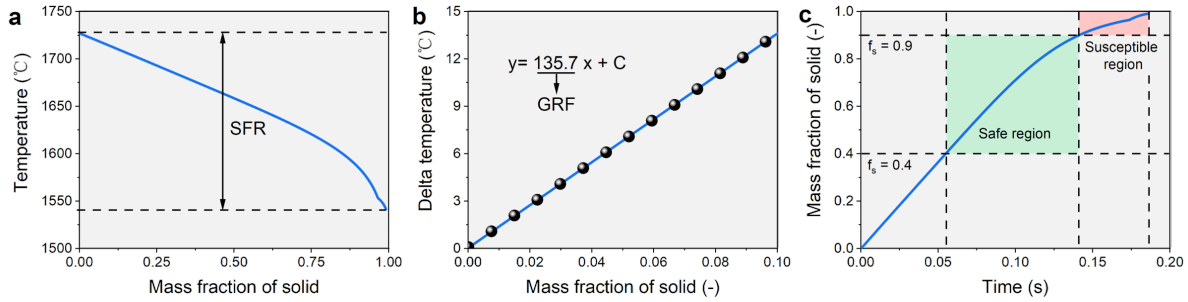

Supplementary Figure 1. A thermodynamic calculation example based on the Scheil model. a Solidification freezing range (*SFR*). **b** Growth restriction factor (*GRF*). **c** Hot cracking susceptibility (*HCS*).

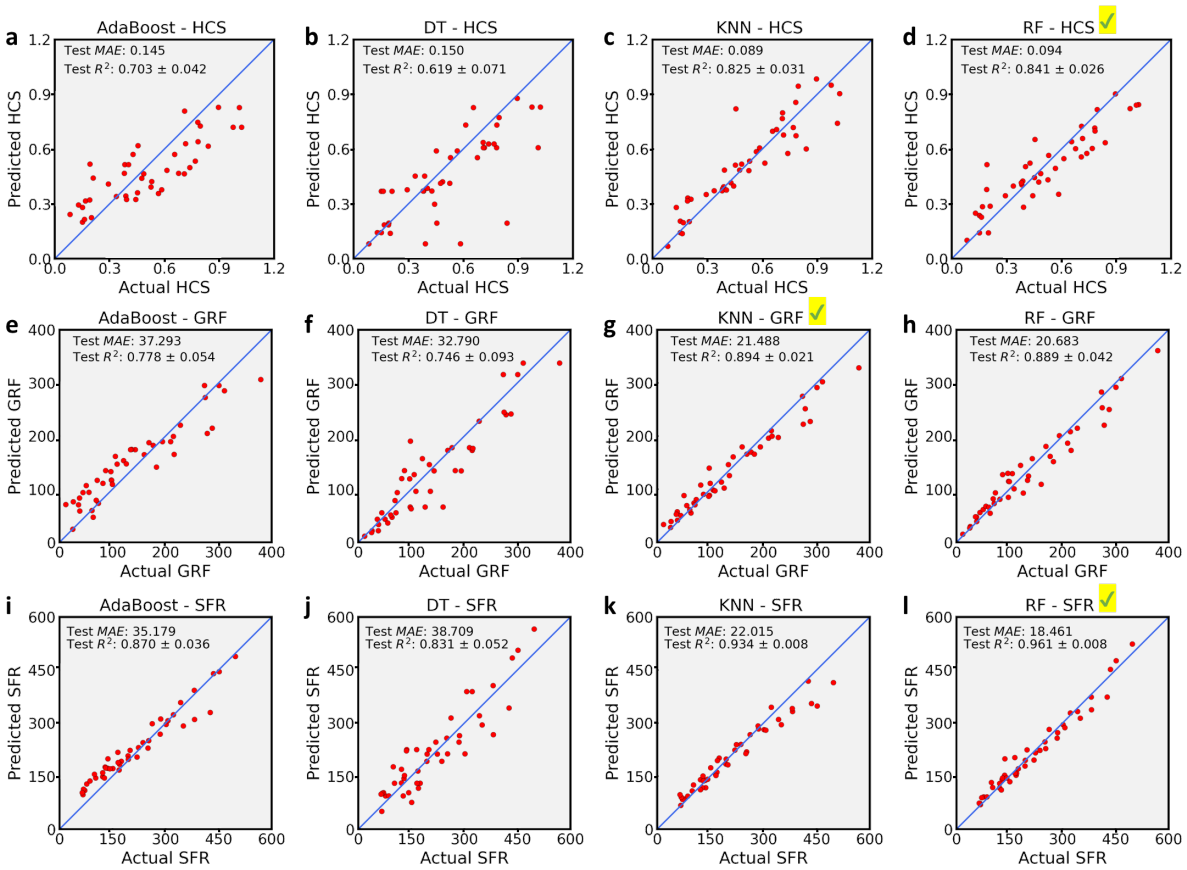

Supplementary Figure 2. Predictive performance of the machine learning surrogate models. a AdaBoost-HCS. **b** DT-HCS. **c** KNN-HCS. **d** RF-HCS. **e** AdaBoost-GRF. **f** DT-GRF. **g** KNN-GRF. **h** RF-GRF. **i** AdaBoost-SFR. **j** DT-SFR. **k** KNN-SFR. **l** RF-SFR. The green tick indicate the optimal model for each factor.

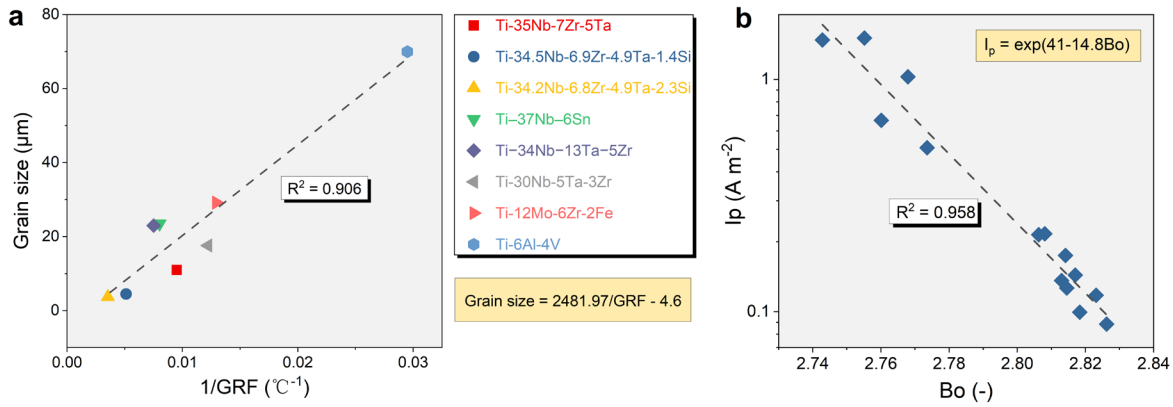

Supplementary Figure 3. Property models in the alloy design framework. a The grain size against the inverse growth restriction factor (*GRF*) for a series of Ti alloys prepared by LPBF. **b** The critical current density for passivation (I_p) against compositional average bond order (*Bo*) (The data points are obtained from corrosion tests of Ti alloys in the 5 wt% HCl solution).

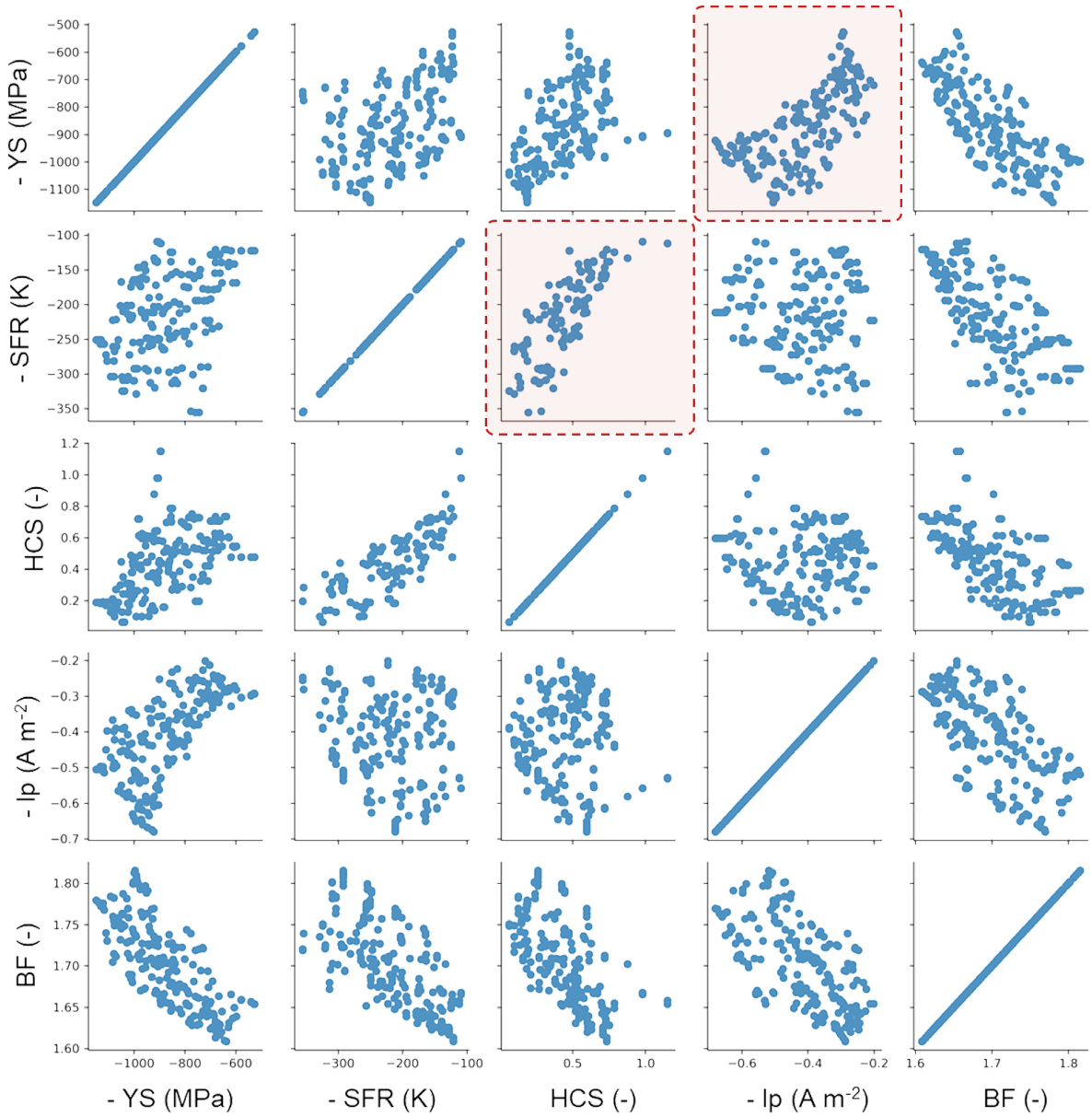

Supplementary Figure 4. Scatter plot matrix of the Pareto front obtained using the non-dominated sorting genetic algorithm II (NSGA-II). A strong positive correlation is observed between *YS* and *Ip*, as well as between -*SFR* and *HCS*.

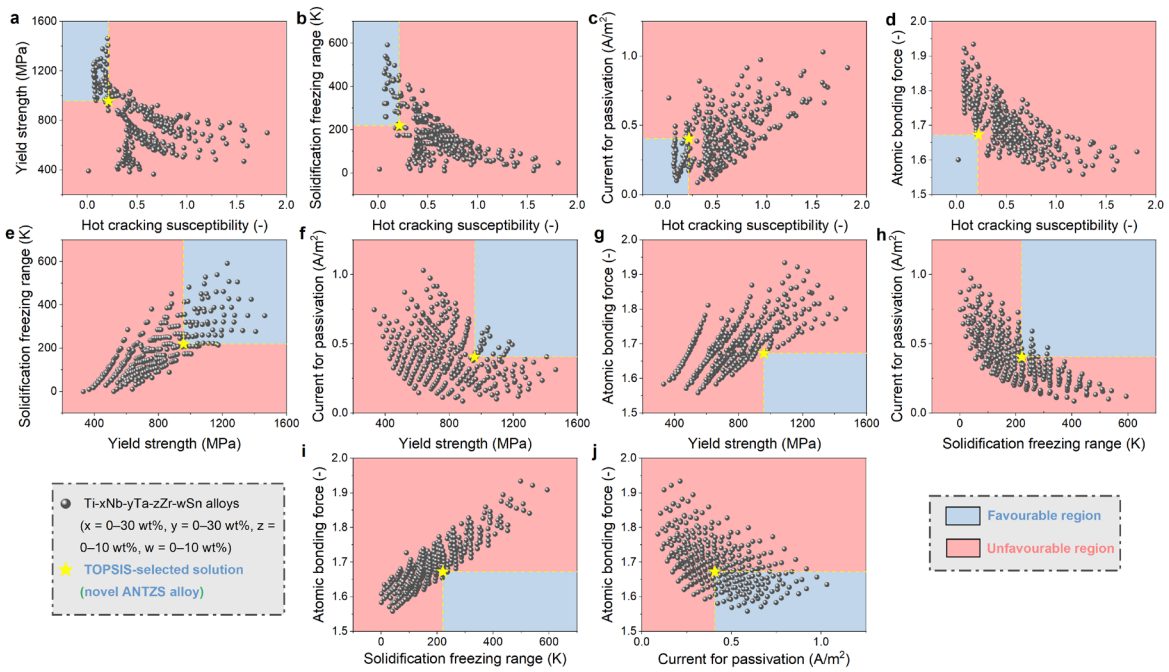

Supplementary Figure 5. Comprehensive properties of the designed ANTZS alloy compared to all the Ti-*x*Nb-*y*Ta-*z*Zr-*w*Sn alloy composition space (within the composition range of *x* = 0–30 wt%, *y* = 0–30 wt%, *z* = 0–10 wt%, and *w* = 0–10 wt%). a Yield strength vs. hot cracking susceptibility. **b** Solidification freezing range vs. hot cracking susceptibility. **c** Passivation current vs. hot cracking susceptibility. **d** Atomic bonding force vs. hot cracking susceptibility. **e** Solidification freezing range vs. yield strength. **f** Passivation current vs. yield strength. **g** Atomic bonding force vs. yield strength. **h** Passivation current vs. solidification freezing range. **i** Atomic bonding force vs. Solidification freezing range. **j** Atomic bonding force vs. Passivation current.

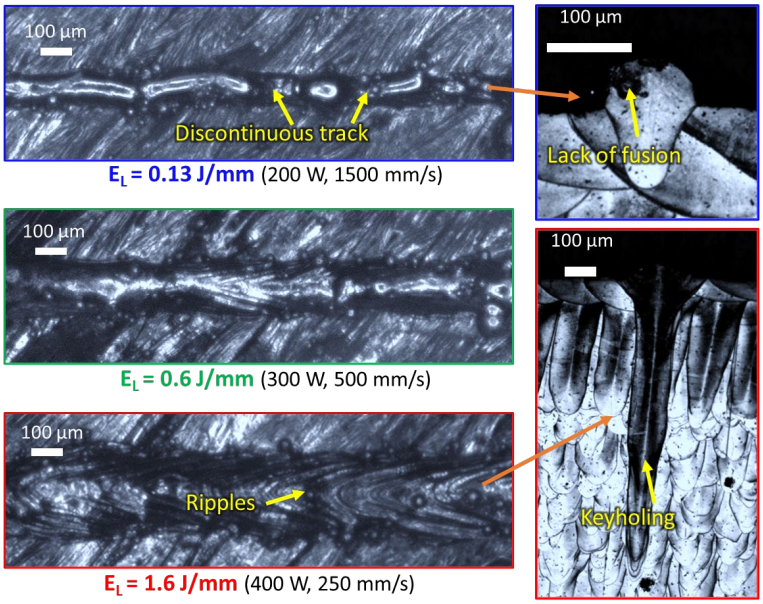

Supplementary Figure 6. LPBF single-track printing of the ANTZS alloy. Typical single-track morphologies with corresponding cross-sectional melt pool images at different linear energy densities (E_L).

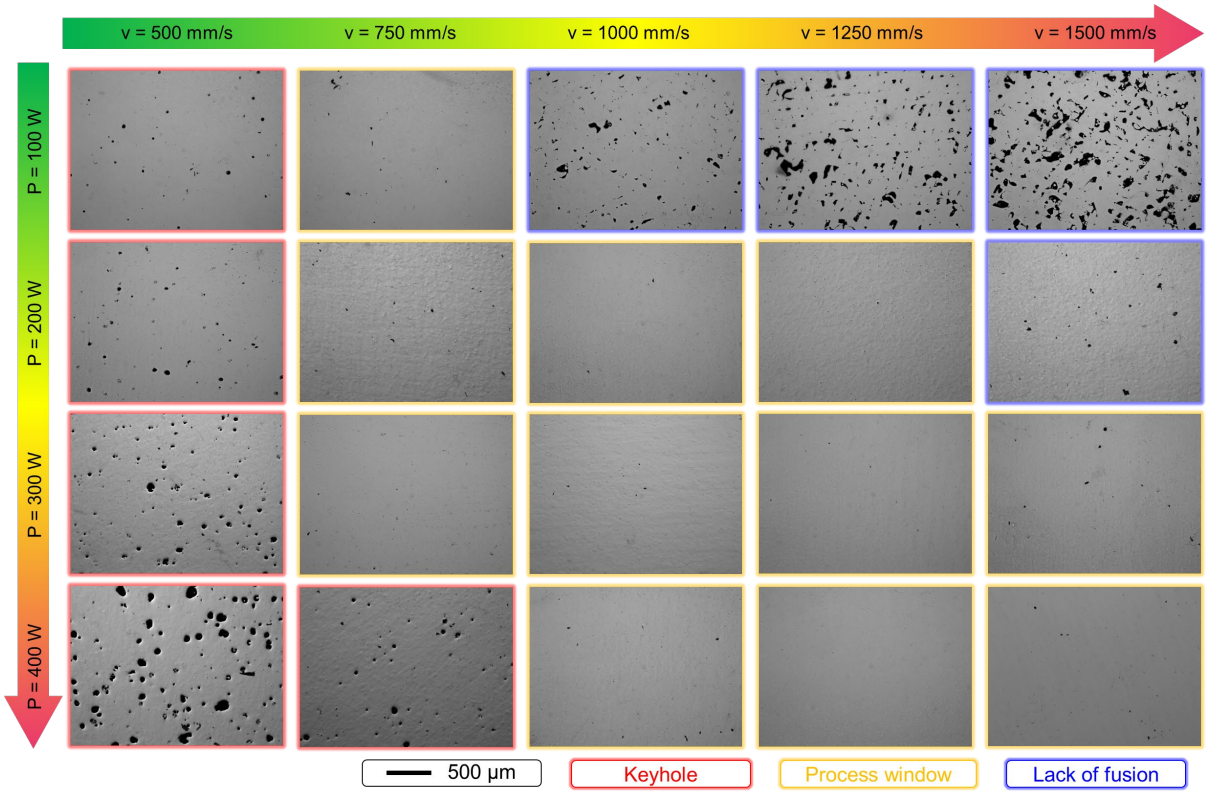

Supplementary Figure 7. Optical microscopy (OM) images of polished cross-sections of LPBF-built ANTZS alloys prepared under varying process parameters. Distinct regions corresponding to lack of fusion (blue), process window (yellow), and keyhole (red) regimes are identified based on pore morphology and relative density.

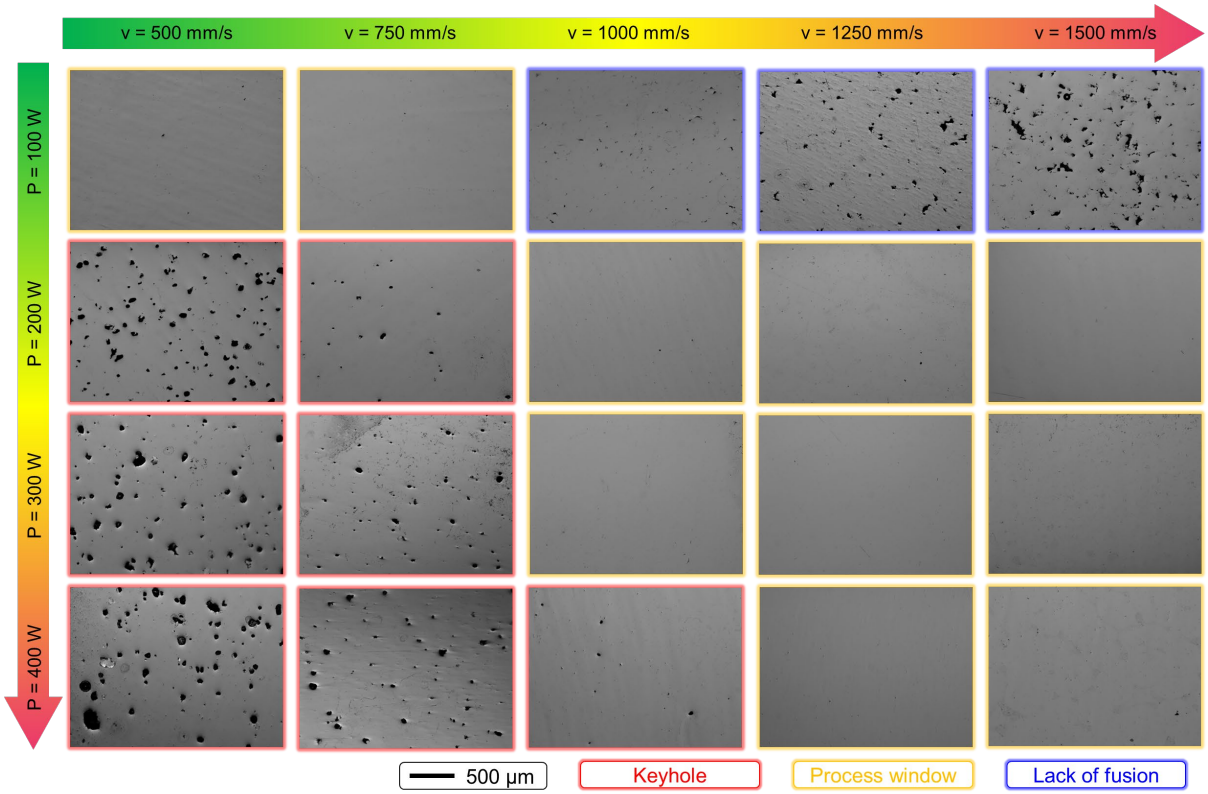

Supplementary Figure 8. Optical microscopy (OM) images of polished cross-sections of LPBF-built Ti64 alloys prepared under varying process parameters. Distinct regions corresponding to lack of fusion (blue), process window (yellow), and keyhole (red) regimes are identified based on pore morphology and relative density.

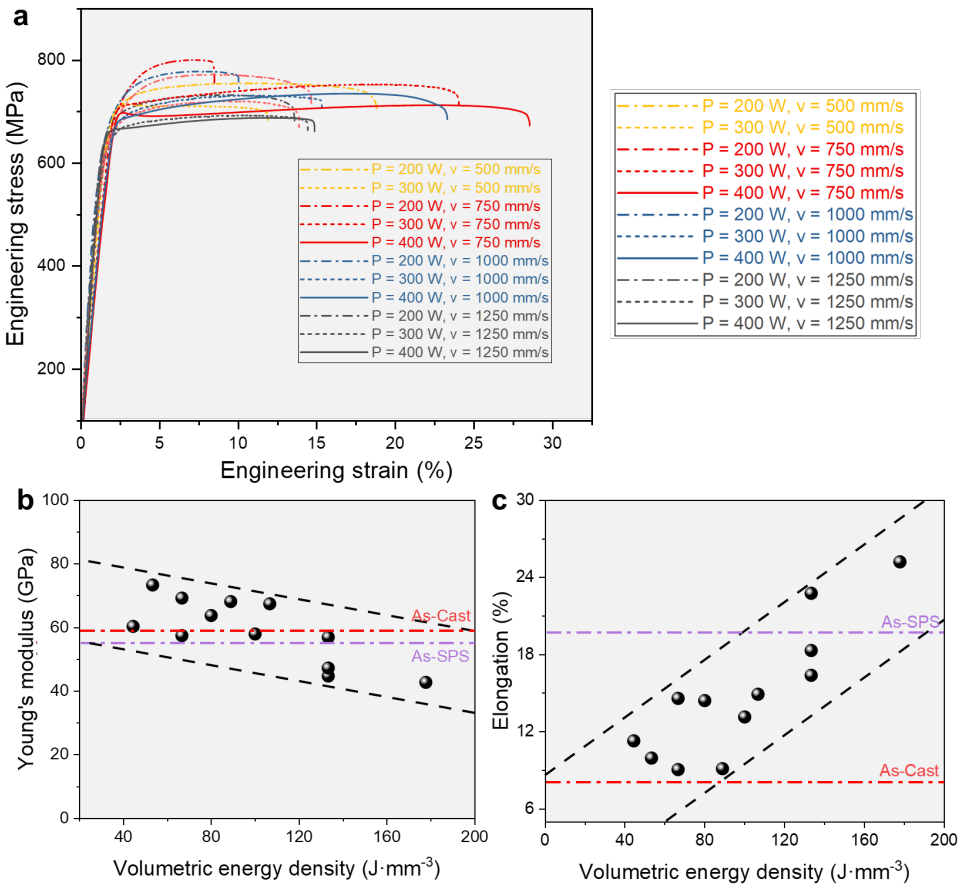

Supplementary Figure 9. Tensile properties of LPBF-built ANTZS alloys fabricated under varying process parameters. a Engineering stress-strain curves of LPBF-built ANTZS alloys (tested along the transverse direction). **b** Young's modulus against volumetric energy density. **c** Elongation against volumetric energy density.

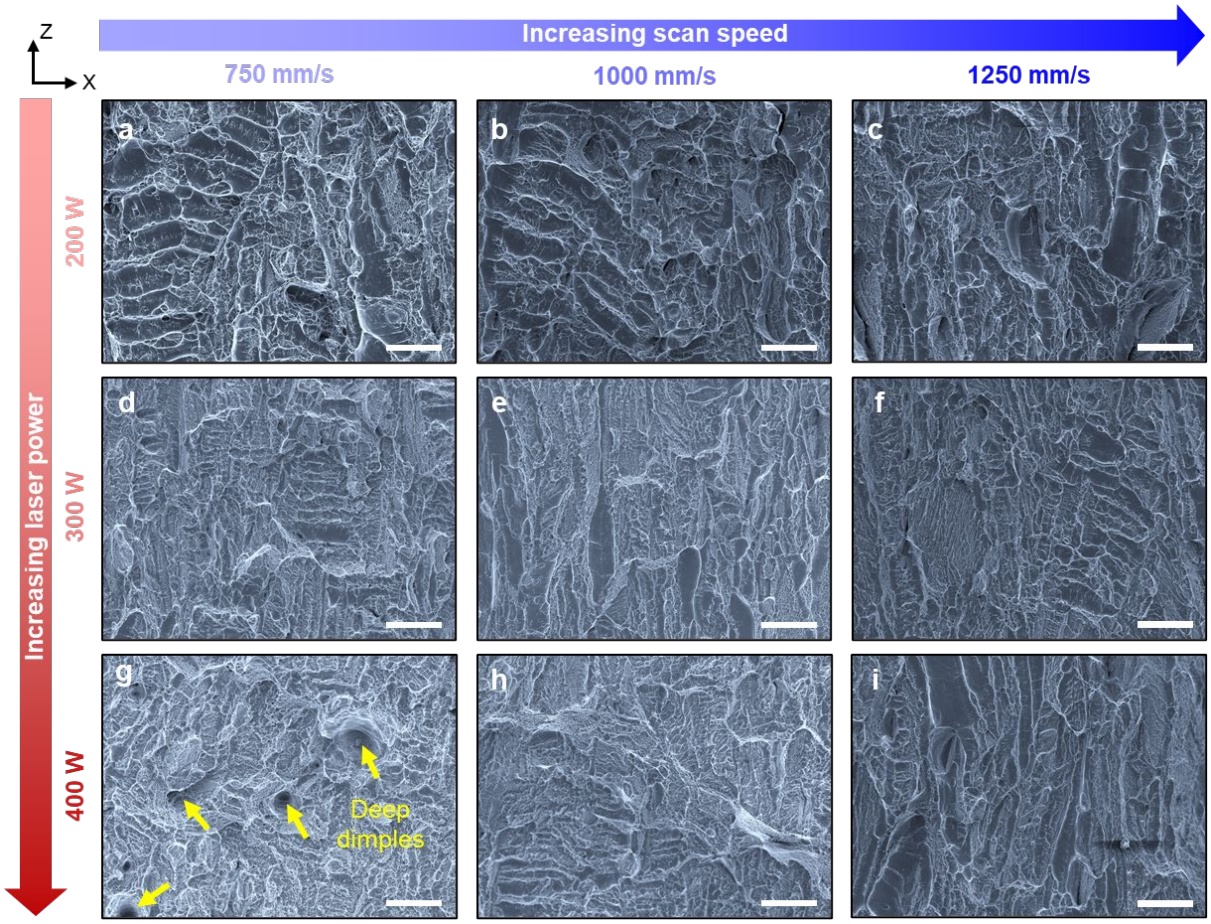

Supplementary Figure 10. Fracture morphologies of LPBF-built ANTZS alloys fabricated under varying process parameters. a 200 W – 750 mm/s. **b** 200 W – 1000 mm/s. **c** 200 W – 1250 mm/s. **d** 300 W – 750 mm/s. **e** 300 W – 1000 mm/s. **f** 300 W – 1250 mm/s. **g** 400 W – 750 mm/s. **h** 400 W – 1000 mm/s. **i** 400 W – 1250 mm/s. (Scale bar = 50 μm)

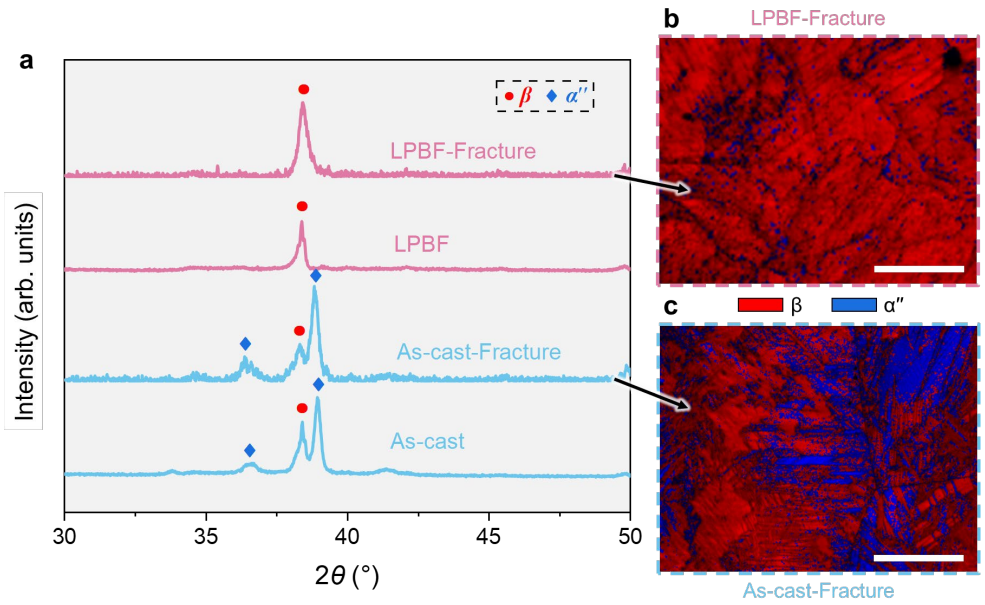

Supplementary Figure 11. Comparison of phase transformation and microstructure evolution in as-cast and LPBF-built ANTZS alloys before and after fracture. a XRD patterns of the alloys in the as-cast, LPBF, and post-fracture states. **b** Phase map of the LPBF ANTZS after fracture. **c** Phase map of the as-cast ANTZS after fracture. (Scale bar = 50 μm)

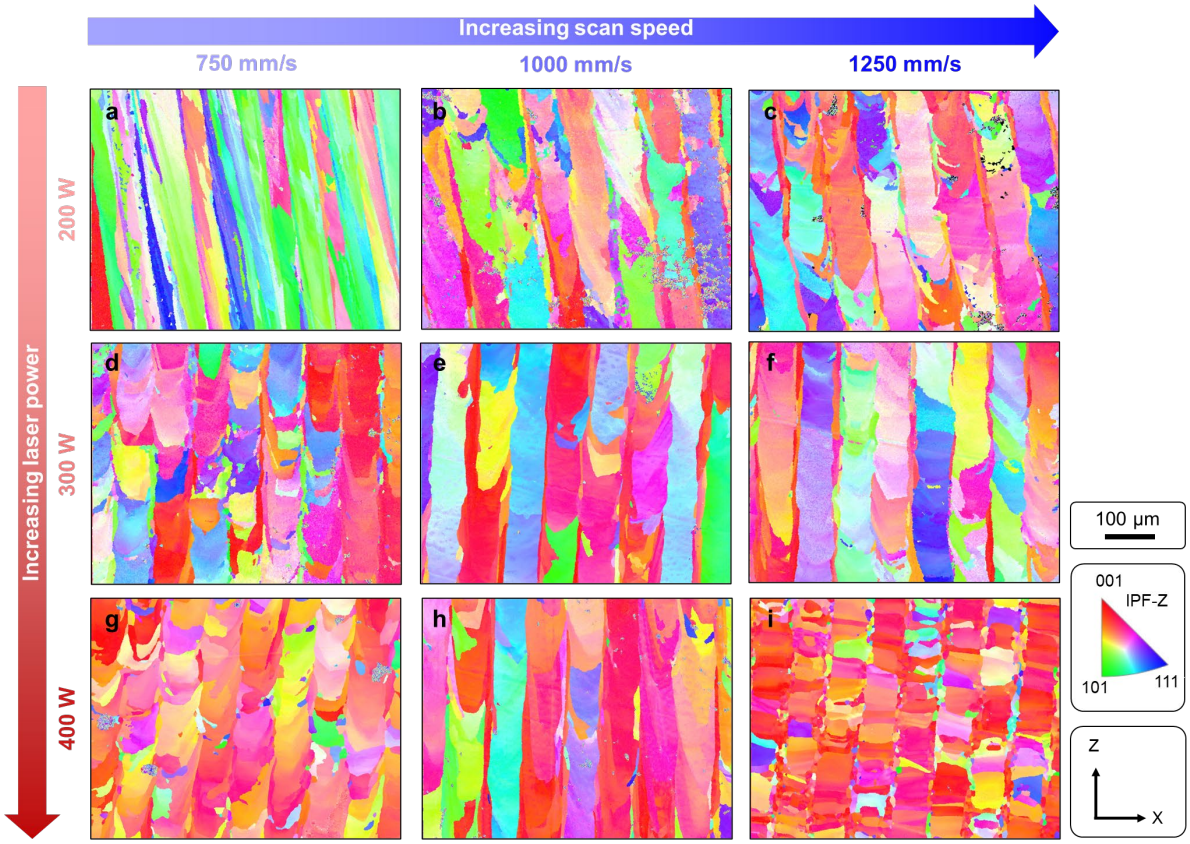

Supplementary Figure 12. EBSD inverse pole figure (IPF) orientation maps of LPBF-built ANZTS alloys fabricated under varying process parameters. a 200 W – 750 mm/s (hit rate = 89.41%). **b** 200 W – 1000 mm/s (hit rate = 77.88%). **c** 200 W – 1250 mm/s (hit rate = 86.44%). **d** 300 W – 750 mm/s (hit rate = 89.77%). **e** 300 W – 1000 mm/s (hit rate = 96.61%). **f** 300 W – 1250 mm/s (hit rate = 92.12%). **g** 400 W – 750 mm/s (hit rate = 98.84%). **h** 400 W – 1000 mm/s (hit rate = 95.75%). **i** 400 W – 1250 mm/s (hit rate = 98.68%). (Scale bar = 100 µm)

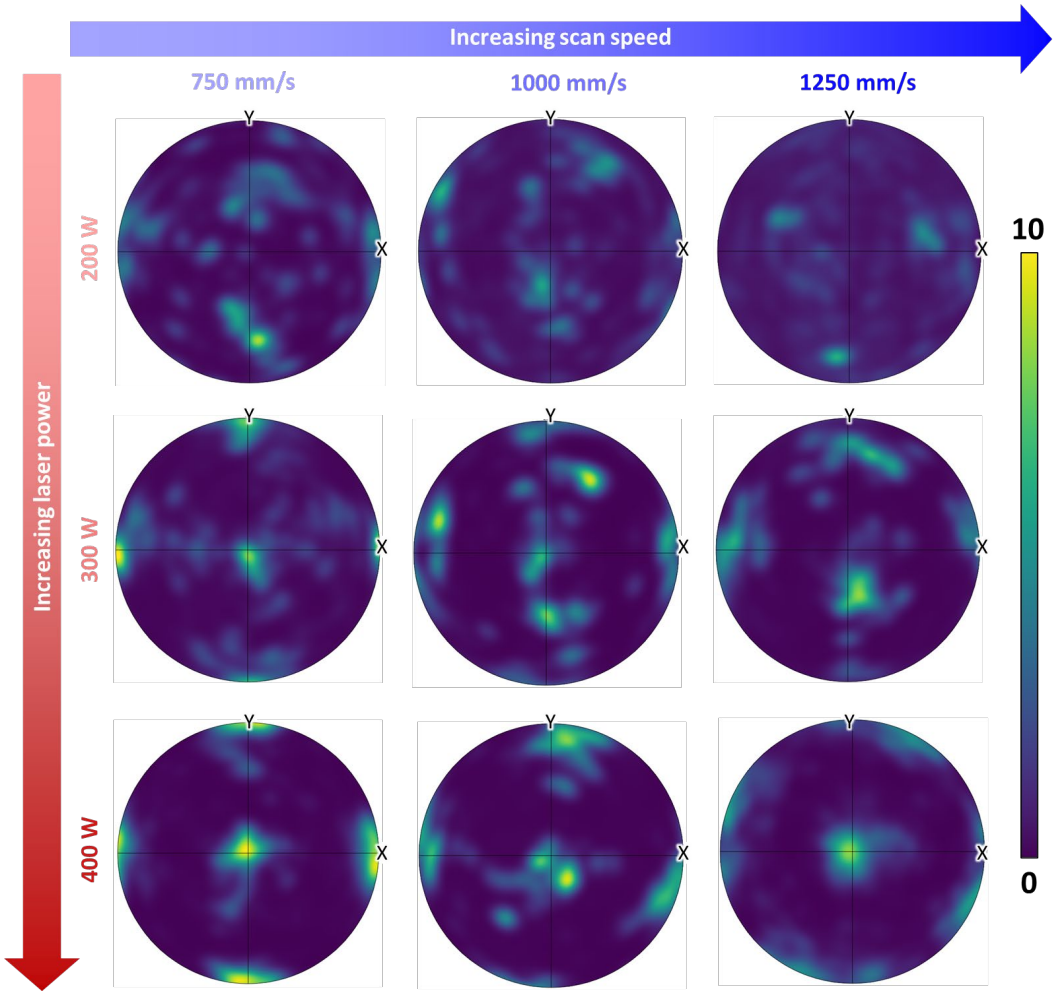

Supplementary Figure 13. Crystallographic texture analysis. (100) pole figures showing the crystallographic texture evolution of ANTZS alloys produced by LPBF at varying combinations of laser power and scan speed.

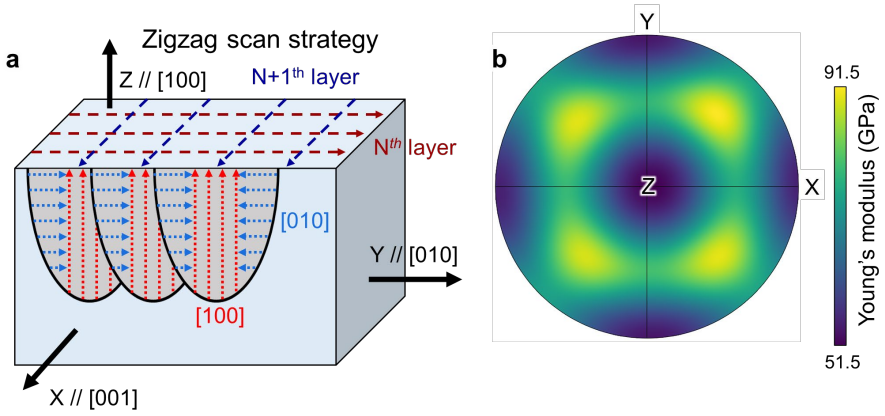

Supplementary Figure 14. Mechanism of low-modulus in LPBF-built ANTZS alloy fabricated under high energy density (P = 400 W, v = 750 mm/s). a Schematic diagram of cubic texture formation. b Loading orientation-dependent Young's modulus of the LPBF ANTZS alloy.

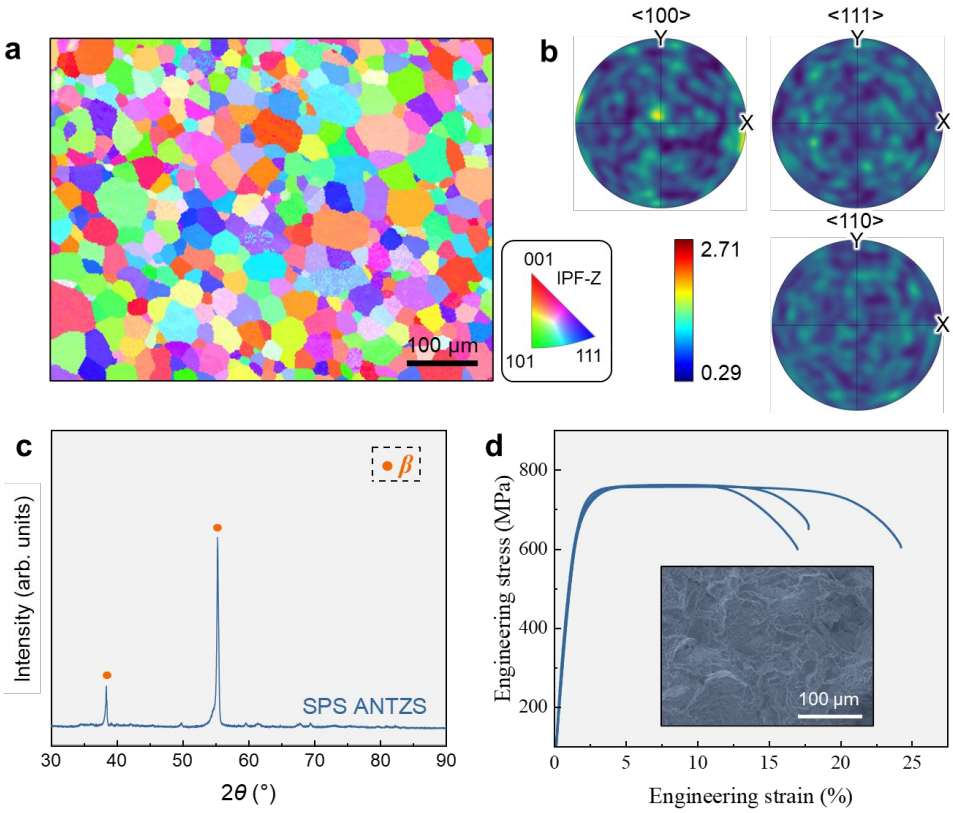

Supplementary Figure 15. Microstructure and mechanical properties of the spark plasma sintering (SPS)-fabricated ANTZS alloy. a IPF orientation map (Z-axis corresponds to the pressure direction). **b** Pole figures. **c** XRD pattern. **d** Engineering stress-strain curves with the fracture morphology.

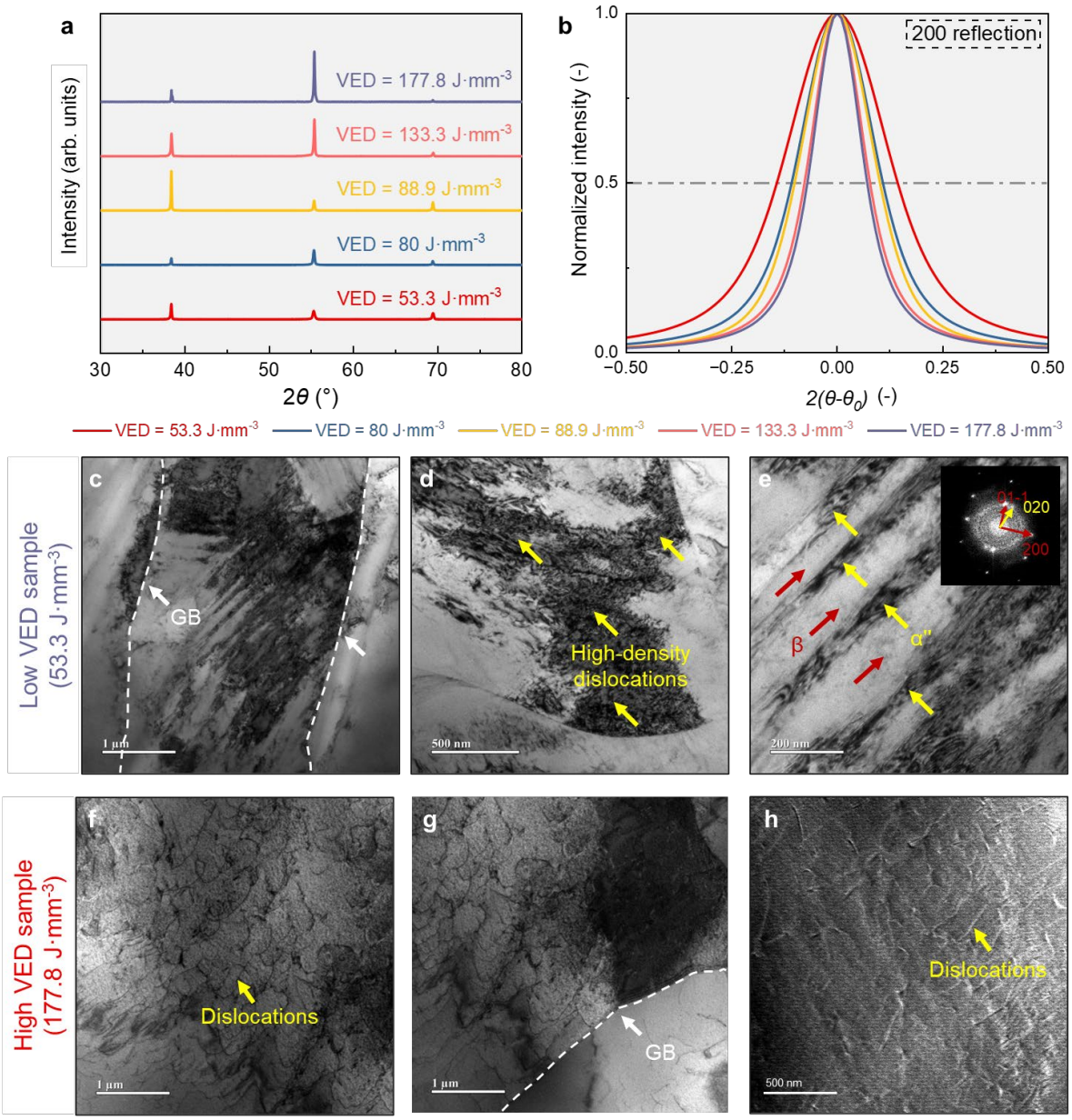

Supplementary Figure 16. Dislocation density evaluation. a XRD patterns of LPBF-fabricated ANTZS alloys under varying volumetric energy densities (different process parameters). **b** Peak broadening of the reflection 200. **c–e** TEM bright-field images of the low VED sample (VED = 53.3 J·mm^{-3}, P = 200 W, v = 1250 mm/s). **f–h** TEM bright-field images of the high VED sample (VED = 177.8 J·mm^{-3}, P = 400 W, v = 750 mm/s).

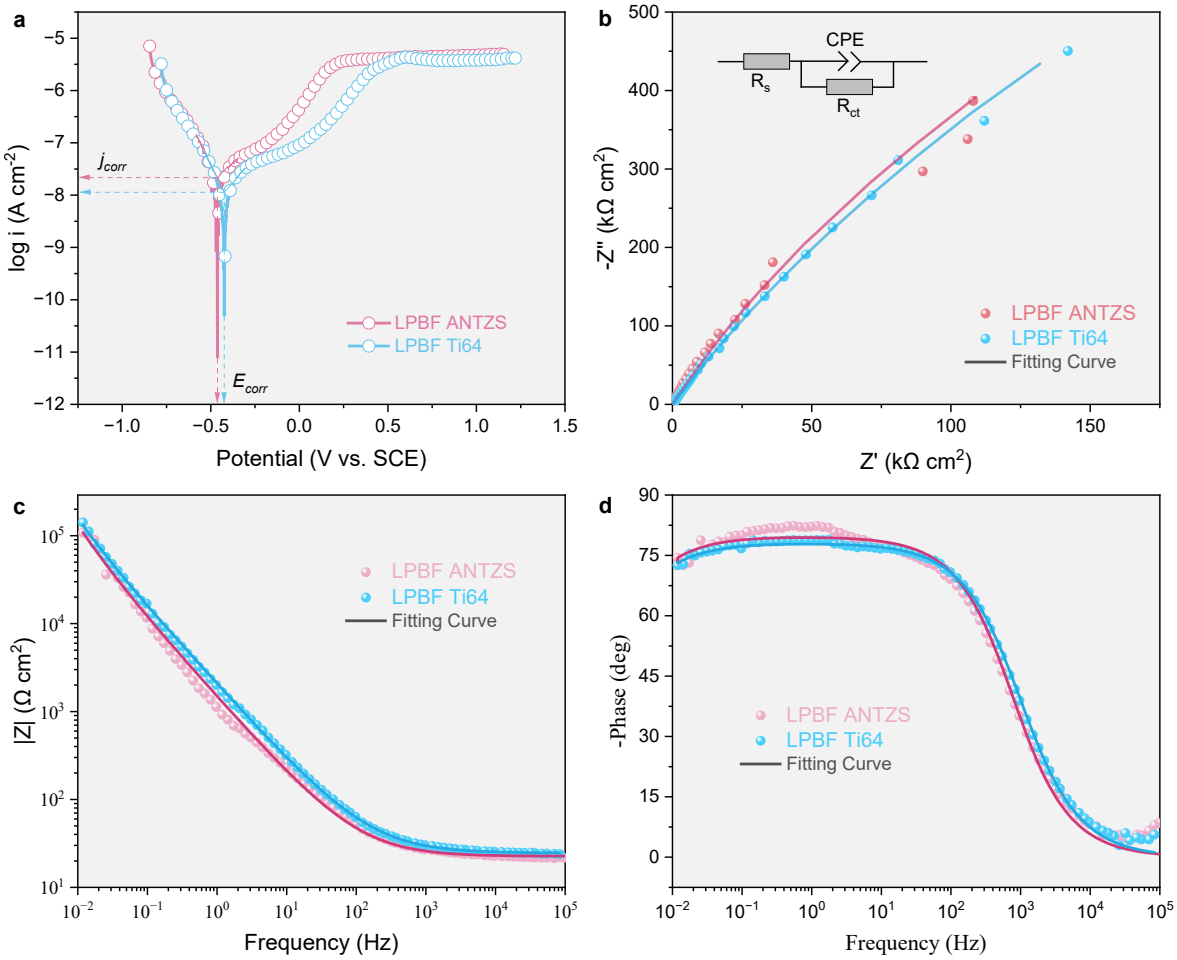

Supplementary Figure17. **Comparative electrochemical corrosion behavior of LPBF ANTZS and Ti64 alloys. a** Potentiodynamic polarization curves of the LPBF ANTZS and LPBF Ti64 alloys in 0.9 wt% NaCl solution. **b** Nyquist plots from electrochemical impedance spectroscopy (EIS). **c** & **d** Bode plots of impedance magnitude and phase angle derived from EIS measurements.

Supplementary Tables

Supplementary Table 1. Hyperparameter tuning of ML surrogate models: search ranges and optimised values.

ML models	Hyperparameters	Range	Optimized values for *HCS*	Optimized values for *GRF*	Optimized values for *SFR*
KNN	n_neighbors, weights	n_neighbors: [5-9], weights: ['uniform', 'distance']	6, distance	4, distance	4, distance
Decision Tree	max_depth	max_depth: [2-6]	6	6	6
AdaBoost	n_estimators	n_estimators: [100-400]	400	300	200
Random Forest	max_depth	max_depth: [1-100]	90	30	30

Supplementary Table 2. *Bo* and *Md* values of the alloying elements.

Element	*Bo* (-)	*Md* (ev)	Z_{eff} (-)
Ti	2.790	2.447	3.4
Nb	3.099	2.424	3.72
Ta	3.144	2.531	3.9
Zr	3.086	2.934	3.4
Sn	2.283	2.100	5.65

Supplementary Table 3. Parameters for the strength models within the alloy design framework.

Parameter	Physical description	Value	Unit
σ_0	Peierls-Nabarro stress of β-Ti	45	MPa
B_{Nb}	Solid solution strengthening coefficient for Nb	71	$MPa \cdot at^{-2/3}$
B_{Ta}	Solid solution strengthening coefficient for Ta	164	$MPa \cdot at^{-2/3}$
B_{Zr}	Solid solution strengthening coefficient for Zr	1201	$MPa \cdot at^{-2/3}$
B_{Sn}	Solid solution strengthening coefficient for Sn	2303	$MPa \cdot at^{-2/3}$
α	Dislocation interaction factor	0.3	-
M_T	Taylor factor	2.6	-
G_m	Shear modulus of β-Ti	39	GPa
b	Burgers vector of β-Ti	0.287	nm
ρ_d	Dislocation density	1.0×10^{15}	m^{-2}
k_{HP}	Hall-Petch factor	0.75	$M \cdot Pam^{1/2}$

Supplementary Table 4. Mechanical properties of ANTZS alloys prepared by different process methods.

Sample	Young's modulus (GPa)	YS (MPa)	UTS (MPa)	ε_u (%)	ε_f (%)
LPBF	42.7 ± 2.1	606.3 ± 3.7	710.9 ± 2.8	17.4 ± 0.6	30.9 ± 3.2
As-cast	58.9 ± 8.5	228.6 ± 8.9	655.4 ± 15.9	5.9 ± 0.3	8.1± 1.3
SPS	55.2 ± 8.4	659.5 ± 9.8	760.4 ± 2.5	8.3 ± 0.1	19.7± 3.2

Supplementary Table 5. Fitted electrochemical parameters obtained from polarization and electrochemical impedance spectroscopy measurements for LPBF ANTZS and LPBF Ti64.

Sample	E_{corr} (V)	i_{corr} (μA·cm^{-2})	*Rs* (Ω)	*CPE-T* (Q)	*CPE-P* (n)	R_{ct} (Ω)
LPBF ANTZS	-0.463	0.0215	22.64	2.403×10^{-5}	0.885	4.35×10^{6}
LPBF Ti64	-0.425	0.0113	24.66	2.053×10^{-5}	0.867	5.15×10^{6}